A fast hybrid simulation approach of ion energy and angular distributions in biased inductively coupled Ar plasmas

Mingliang ZHAO (赵明亮)**, Yuru ZHANG** (张钰如)[*]**, Fei GAO** (高飞) **and Younian WANG** (王友年)

Key Laboratory of Materials Modification by Laser, Ion, and Electron Beams (Ministry of Education), School of Physics, Dalian University of Technology, Dalian 116024, People's Republic of China

E-mail: yrzhang@dlut.edu.cn

CrossMark

Abstract

In this work, a two-dimensional hybrid model, which consists of a bulk fluid module, a sheath module and an ion Monte-Carlo module, is developed to investigate the modulation of ion energy and angular distributions at different radial positions in a biased argon inductively coupled plasma. The results indicate that when the bias voltage amplitude increases or the bias frequency decreases, the ion energy peak separation width becomes wider. Besides, the widths of the ion energy peaks at the edge of the substrate are smaller than those at the center due to the lower plasma density there, indicating the nonuniformity of the ion energy distribution function (IEDF) along the radial direction. As the pressure increases from 1 to 10 Pa, the discrepancy of the IEDFs at different radial positions becomes more obvious, i.e. the IEDF at the radial edge is characterized by multiple low energy peaks. When a dual frequency bias source is applied, the IEDF exhibits three or four peaks, and it could be modulated efficiently by the relative phase between the two bias frequencies. The results obtained in this work could help to improve the radial uniformity of the IEDF and thus the etching process.

(Some figures may appear in colour only in the online journal)

1. Introduction

Inductively coupled plasmas (ICPs) are widely used in integrated circuit fabrication for etching and deposition processes [1, 2]. One of the most attractive advantage of ICPs is that the ion energy and ion flux can in principle be controlled independently by applying a radio frequency (RF) or direct current (DC) bias source to the substrate [3]. Indeed, ion energy and angular distributions (IEADs) at the substrate are of significant importance for etching process, because IEADs directly affect the etch rate, etch anisotropy, etc [4]. In order to optimize the etching process, stringent requirements have been put forward for the modulation of IEADs.

As an important research method, numerical simulation is widely used in the investigation of IEADs in ICPs because of its low cost, high efficiency, as well as the ability to output more physical information. A global model, which can be used to simulate discharges with complex chemical reactions [5–8], is usually combined with a sheath model and an ion Monte-Carlo collision (MCC) model to study the IEADs in ICPs. For example, Haidar et al investigated the ion energy distribution functions (IEDFs) in inductively coupled SF_6 and C_4F_8 plasmas, and they found that the ion energy peak separation width of SF_6 plasma was narrower than that of C_4F_8 plasma under the same discharge condition, due to the higher electronegativity and thinner sheath in SF_6 discharges [9]. By taking the influence of the sheath on the plasma bulk into account, Wen et al presented that the plasma density first decreased and then increased with bias amplitude, and the

---

[*] Author to whom any correspondence should be addressed.

width of the ion energy peaks became wider at higher bias voltage, which was consistent with experimental results [10]. Moreover, Tong *et al* focused on Cl$_2$ ICP discharges, and they concluded that as the bias amplitude increased, the IEADs of Cl$_2^+$ and Cl$^+$ moved towards the high-energy region, and the ion energy peak separation width increased [11].

Although the hybrid simulation approach based on the global model can be used to investigate the biased ICP efficiently, the spatial distributions of the plasma parameters are unavailable, which limits its application. Therefore, a fluid model for plasma region is necessary for studying the biased ICP, as well as the IEADs. Kawamura *et al* coupled a fast fluid model for bulk region with a single-frequency analytical sheath model, which could simulate biased Ar ICPs within 30 min [12]. Zhang *et al* combined a two-dimensional (2D) fluid model with a one-dimensional (1D) numerical sheath model to study the IEADs at the center of the plate in Ar/O$_2$ ICPs [13], and they revealed that as the oxygen content increased, the ion energy peaks shifted towards the high-energy region, and the ions were better collimated. By using the hybrid plasma equipment model (HPEM) [14], Hoekstra *et al* showed that the IEDF of Cl$_2^+$ near the radial edge of the wafer was much narrower than that at the radial center in an Ar/Cl$_2$ inductively coupled plasma [15]. Agarwal *et al* used HPEM to investigate the influence of the non-sinusoidal bias on the IEDF, and they demonstrated that the tailored bias voltage waveform could reduce the sensitivity of the IEDF to the ion mass [16].

Although many modelling works have been done on the IEADs and sheath effect in biased ICPs, there still exist some problems. For instance, most of the previous works only capture the IEADs at the substrate center, but the ion properties at different positions are hardly considered. Furthermore, the investigation of the influence of bias voltage waveforms on the IEADs in ICPs is limited. Therefore, a hybrid model, which deals with the plasma bulk and the sheath separately, is developed in this work. By running the 1D fluid sheath model at different radial positions based on the plasma properties provided by the 2D bulk plasma model, the IEADs above the entire electrode under various discharge conditions (i.e. bias voltage, bias frequency, pressure and bias voltage waveform) in Ar plasmas are studied.

This paper is organized as follows. In section 2, the hybrid model is described in detail. In section 3, we first prove the validity of the hybrid model, and then the modulations of IEADs by single-frequency bias and dual-frequency bias are investigated, respectively. Finally, a brief conclusion is given.

2. Hybrid model

The schematic diagram of the biased ICP reactor is shown in figure 1. The chamber is cylindrical, with a radius of 15 cm and a height of 10 cm. A two-turn radio frequency (RF) coil is placed over the dielectric window, whose thickness is 1.2 cm, and the radial positions of the coil are 6 cm and 8 cm from the
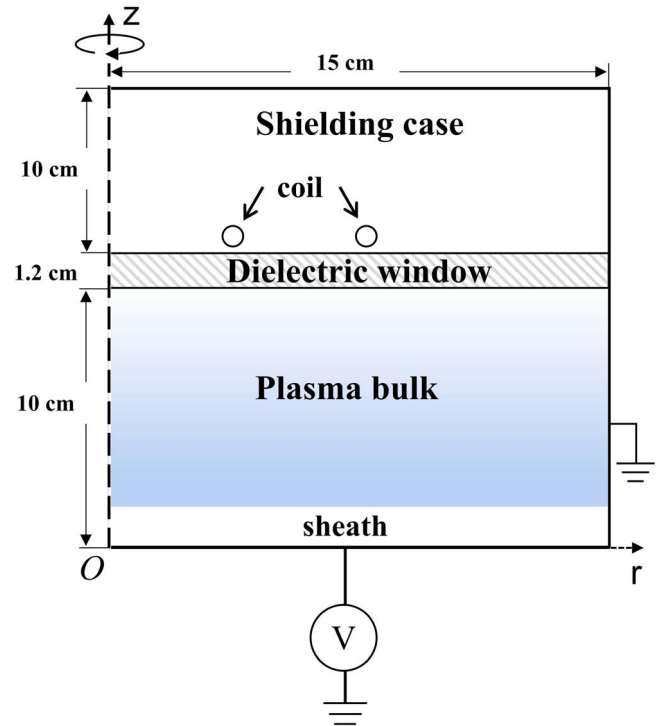

Figure 1. Schematic diagram of a biased planer ICP reactor.

symmetric axis. An RF bias source is applied to the substrate to modulate the IEAD there.

The hybrid model for Ar discharges used in this study consists of a plasma module, a sheath module, an electromagnetic module, and an ion Monte-Carlo collision (MCC) module.

2.1. Plasma module

Since the thickness of the sheath is much smaller than the height of the chamber, a strong spatial stiffness is unavoidable if the plasma bulk and the sheath region are simulated together. To overcome this numerical difficulty, the bulk and the sheath are treated separately in this work, i.e. a modified ambipolar diffusion model (MADM) is adopted for the bulk region [17], and the oscillation of the sheath is numerically described by a 1D fluid sheath model. In order to demonstrate the accuracy and efficiency of this hybrid model, a comparison with other models, namely ambipolar diffusion model (ADM) and two-fluid model (TFM), has been presented in section 2.1 below.

2.1.1. Ambipolar diffusion model and modified ambipolar diffusion model. ADM is one of the commonly used models for ICPs, due to its high computational efficiency [12, 18, 19]. In this model, the electron density is determined by the quasi-neutral condition, which is a good assumption for high-density plasmas

$$en_e = q_i n_i. \tag{1}$$

Here, e is the unit charge, n_e is the electron density, q_i and n_i are the charge and density of ions. Due to the small electron

mass, the electron flux satisfies the drift diffusion approximation

$$\mathbf{\Gamma}_e = -\mu_e n_e \mathbf{E}_s - D_e \nabla n_e, \qquad (2)$$

where μ_e is the electron mobility, D_e is the electron diffusion coefficient, and $\mathbf{E}_s$ is the ambipolar electrostatic field.

The electron temperature T_e is obtained by solving the energy balance equation

$$\frac{\partial}{\partial t}\left(\frac{3}{2}n_e k_B T_e\right) + \nabla \cdot \mathbf{Q}_e = -e\mathbf{\Gamma}_e \cdot \mathbf{E}_s + P_{ind} - \sum_j \varepsilon_j, \quad (3)$$

where k_B is the Boltzmann constant, $\mathbf{Q}_e$ is the electron energy flux, ε_j is the energy loss due to inelastic collisions. P_{ind} is the inductive power density

$$P_{ind} = \frac{1}{2}\operatorname{Re}(J_\theta E_\theta^*), \qquad (4)$$

where J_θ and E_θ are the azimuthal electron current density and azimuthal inductive electric field, respectively, which are calculated by the electromagnetic module below.

The ion density is governed by the ion continuity equation

$$\frac{\partial n_i}{\partial t} + \nabla \cdot \mathbf{\Gamma}_i = S_i, \qquad (5)$$

where S_i is the ion source term, and the ion flux $\mathbf{\Gamma}_i$ also satisfies the drift diffusion approximation

$$\mathbf{\Gamma}_i = \mu_i n_i \mathbf{E}_s - D_i \nabla n_i, \qquad (6)$$

where μ_i is the ion mobility and D_i is the ion diffusion coefficient.

Since only the bulk region is simulated, the Poisson equation is not needed in the ADM, and the ambipolar electrostatic field in the bulk region is obtained by using $\mathbf{\Gamma}_e = \mathbf{\Gamma}_i$

$$E_s = -\frac{D_e - D_i}{\mu_e + \mu_i}\frac{\nabla n_i}{n_i}. \qquad (7)$$

Because the inertia of ions is only negligible at high pressures [20], the validity of the ADM at low pressures is limited. Therefore, the ADM has been modified, i.e. MADM [17]. In the MADM, the drift diffusion approximation for the ion flux is replaced by the ion momentum balance equation for the ion velocity $\mathbf{u}_i$

$$\frac{\partial(n_i m_i \mathbf{u}_i)}{\partial t} + \nabla \cdot (n_i m_i \mathbf{u}_i \mathbf{u}_i) = n_i q_i \mathbf{E}_s - k_B T_i \nabla n_i + \mathbf{M}_i,$$
$$(8)$$

where m_i is the ion mass, and $\mathbf{M}_i$ represents the momentum transfer between ions and neutral particles by collisions. T_i is the ion temperature, which is assumed to be 330 K in this work. An explicit time advancement scheme is adopted, and the upwind scheme is employed to discretize the ion momentum balance equation. Again, by assuming that the electron flux is equal to the ion flux, the ambipolar

electrostatic field in the plasma bulk is determined

$$\mathbf{E}_s = -\frac{n_i \mathbf{u}_i + D_e \nabla n_e}{\mu_e n_e}. \qquad (9)$$

This modification makes the MADM suitable for both low pressure and high pressure.

For neutral species, the continuity equation is

$$\frac{\partial n_n}{\partial t} + \nabla \cdot (-D_n \nabla n_n) = S_n, \qquad (10)$$

where n_n, D_n and S_n are the density, diffusion coefficient and source term for neutral species.

2.1.2. Two-fluid model. The validity of the MADM has been proved by comparing with the TFM [20, 21]. In the TFM, both the bulk region and the sheath region are simulated self-consistently, which is the main difference between the MADM and the TFM. Here, the electron density is obtained by solving the continuity equation

$$\frac{\partial n_e}{\partial t} + \nabla \cdot \mathbf{\Gamma}_e = S_e, \qquad (11)$$

where S_e is the electron source term. The equations for the electron flux, electron temperature, ion density, ion velocity and neutral particle density are the same as those in the MAMD.

Since the sheath region is considered, the electric potential V and the electrostatic field $\mathbf{E}_s$ are calculated by the Poisson equation

$$\nabla \cdot (\varepsilon_0 \nabla V) = -(q_i n_i - e n_e). \qquad (12)$$

$$\mathbf{E}_s = -\nabla V, \qquad (13)$$

where ε_0 is the vacuum permittivity.

2.1.3. Boundary conditions. To solve the above fluid equations, boundary conditions are necessary. In ADM and MADM, the boundary condition for the ion density at the chamber wall is $\nabla n_i \cdot \mathbf{e}_n = 0$, and the ion flux is $\Gamma_i = n_i u_B$, where u_B is the ion Bohm velocity. For the electron energy flux, it is $\mathbf{Q}_e = \frac{5}{2}k_B T_e \mathbf{\Gamma}_e$ at the walls, and it is set to 0 at the symmetry axis. Note that the stochastic heating flux is considered at the bottom bulk-sheath interface in AMD and MADM, as indicated by equation (26) below. For neutral species, the boundary condition is $\Gamma_n = \frac{1}{4}n_n \sqrt{\frac{8k_B T_g}{\pi m_g}}$, where Γ_n is the neutral flux at the walls, $T_g = 330$ K is the neutral temperature and m_g is the mass of neutral particles.

In TFM, the electron flux perpendicular to the chamber wall satisfies $\mathbf{\Gamma}_{en} = \pm\frac{1}{4}n_{e,boundary}v_{th}$, where v_{th} is the average thermal velocity for electrons, $n_{e,boundary}$ is the electron density at the boundaries, and the radial component of the electron flux at the symmetry axis is $\Gamma_{er} = 0$. The ion density at the boundaries is continuous, and the ion velocity is obtained by extrapolation. Besides, the potential at the walls is 0, and $\frac{\partial V}{\partial r} = 0$ is satisfied at the axis of symmetry.

2.2. Electromagnetic module

The electromagnetic fields in ICP discharges are determined by the Maxwell equations

$$\nabla \times \mathbf{E} = -\frac{\partial \mathbf{B}}{\partial t}, \tag{14}$$

$$\nabla \times \mathbf{B} = \mu_0(\mathbf{J}_\text{p} + \mathbf{J}_\text{coil}) + \mu_0\varepsilon\frac{\partial \mathbf{E}}{\partial t}. \tag{15}$$

Here, $\mathbf{E}$ is the inductive electric field, $\mathbf{B}$ is the inductive magnetic field, $\mathbf{J}_\text{coil}$ is the current density of the coil, μ_0 is the permeability of vacuum, and ε is the permittivity. The plasma current density $\mathbf{J}_\text{p}$ is given by

$$\frac{\partial \mathbf{J}_\text{p}}{\partial t} = \frac{e^2 n_\text{e}}{m_\text{e}}\mathbf{E} - v_\text{en}\mathbf{J}_\text{p}, \tag{16}$$

where m_e is the electron mass, and v_en is the elastic collision frequency between electrons and neutral particles. Substituting equations (15) and (16) into the curl of equation (14), we have

$$\nabla^2\mathbf{E} - \mu_0\varepsilon\frac{\partial^2\mathbf{E}}{\partial t^2} = \mu_0\frac{\partial \mathbf{J}_\text{p}}{\partial t} + \mu_0\frac{\partial \mathbf{J}_\text{coil}}{\partial t}. \tag{17}$$

In this work, we assume that the discharge works in the H mode, so the inductive electric field only has angular component E_θ. According to the harmonic approximation, the real part $E_{\theta\text{r}}$ and imaginary part $E_{\theta\text{i}}$ are

$$\omega\mu_0\sigma_\text{r}E_{\theta\text{i}} + (\omega\mu_0\sigma_\text{i} - \mu_0\varepsilon\omega^2)E_{\theta\text{r}} = \nabla^2 E_{\theta\text{r}} - \frac{E_{\theta\text{r}}}{r^2}, \tag{18}$$

$$-\omega\mu_0\sigma_\text{r}E_{\theta\text{r}} + (\omega\mu_0\sigma_\text{i} - \mu_0\varepsilon\omega^2)E_{\theta\text{i}} - \omega\mu_0 J_\text{coil}$$
$$= \nabla^2 E_{\theta\text{i}} - \frac{E_{\theta\text{i}}}{r^2}, \tag{19}$$

where ω is the angular frequency of the coil, $\sigma_\text{r} = e^2 n_\text{e} v_\text{en}/m_\text{e}(v_\text{en}^2 + \omega^2)$ and $\sigma_\text{i} = e^2 n_\text{e}\omega/m_\text{e}(v_\text{en}^2 + \omega^2)$ are the real part and imaginary part of the plasma conductivity, respectively. Note that in the simulation, the magnitude of the coil current density is adjusted according to the fixed total absorbed power. The chamber walls are assumed to be perfect conductors, so $\mathbf{E}_\theta$ is equal to zero at the boundaries. Besides, $\mathbf{E}_\theta$ is zero at the axis due to axial symmetry.

2.3. Sheath module

As we mentioned above, the ADM and MADM can only describe the bulk plasma properties. Therefore, a sheath module is necessary to describe the sheath dynamics [22–26] and complete the model. In this work, a 1D numerical sheath model, which solves fluid equations and the Poisson equation

self-consistently [25, 26], is adopted to study the sheath characteristics induced by arbitrary bias voltage waveforms.

The electron density in the sheath $n_\text{e,sheath}(x)$ is assumed to satisfy the Boltzmann relation

$$n_\text{e,sheath}(x) = n_0 \exp\left(\frac{e(V(x) - V_0)}{k_\text{B}T_\text{e}}\right). \tag{20}$$

Here, n_0 is the electron density at the bulk-sheath interface provided by the plasma module, and V_0 is the potential there, which is set to 0. The electric potential in the sheath $V(x)$ is governed by the Poisson equation, and the electron temperature in the sheath is assumed to equal the value at the bulk-sheath interface. The behavior of ions is described by the 1D continuity equation and momentum balance equation.

When a bias source is applied, the voltage on the bottom electrode is

$$V_\text{bias}(t) = \begin{cases} V_1\sin(\omega_1 t) + V_\text{DC} & \text{for single frequency bias source,} \\ V_1\sin(\omega_1 t) + V_2\sin(\omega_2 t + \phi) + V_\text{DC} & \text{for dual frequency bias source.} \end{cases} \tag{21}$$

Here, V_1 and V_2 are the amplitudes for frequencies ω_1 and ω_2, and ϕ is the relative phase between them.

V_DC is the DC self-bias voltage, which is determined by an analytical method instead of the equivalent circuit model [25, 26], to avoid the time-consuming iteration process. According to the current conservation law, we have

$$I_\text{i} - I_\text{e} + I_\text{d} = I_\text{RF}. \tag{22}$$

Here, $I_\text{i} = Aen_0 u_\text{B}$ is the ion current, $I_\text{e} = \frac{1}{4}en_0 \exp[eV_\text{bias}(t)/k_\text{B}T_\text{e}]v_\text{th}A$ is the electron current, I_d is the displacement current, I_RF is the total current flowing though the sheath, A is the electrode area, $u_\text{B} = (k_\text{B}T_\text{e}/m_\text{i})^{1/2}$ is the Bohm velocity, $v_\text{th} = (8k_\text{B}T_\text{e}/\pi m_\text{e})^{1/2}$ is the electron average thermal velocity. Taking the average of equation (22) over one RF period, we have [3]

$$\frac{1}{4}v_\text{th}\left\langle \exp\left[\frac{eV_\text{bias}(t)}{k_\text{B}T_\text{e}}\right]\right\rangle = u_\text{B}. \tag{23}$$

Substituting $V_\text{bias}(t)$ into equation (23), the DC self-bias voltage V_DC is determined. For single frequency bias source [3]

$$V_\text{dc} = \frac{1}{2}\frac{k_\text{B}T_\text{e}}{e}\ln\left(\frac{2\pi m_\text{e}}{m_\text{i}}\right) - \frac{k_\text{B}T_\text{e}}{e}\ln\left(I_0\left(\frac{eV_1}{k_\text{B}T_\text{e}}\right)\right), \tag{24}$$

where I_0 is zero-order modified Bessel function. For dual frequency bias source, it is difficult to get the analytical expression of V_DC. Therefore, V_DC is calculated numerically

$$V_\text{dc} = \frac{k_\text{B}T_\text{e}}{e}\ln\left(\frac{1}{C}\sqrt{\frac{2\pi m_\text{e}}{m_\text{i}}}\right), \tag{25}$$

where $C = \frac{1}{T}\int_0^T \exp\left[\frac{e(V_1\sin(\omega_1 t) + V_2\sin(\omega_2 t + \phi))}{k_\text{B}T_\text{e}}\right]dt$, and T is the period of the bias source.

Table 1. Reactions for Ar discharges in the hybrid model.

NO.	Reactions	Rate coefficients (m^3 s^{-1})	References
1	e + Ar → e + Ar	$2.336 \times 10^{-14} T_e^{1.609} \exp\left(\begin{array}{c} 0.0618(\ln T_e)^2 \\ -0.1171(\ln T_e)^3 \end{array}\right)$	[1]
2	e + Ar → e + Ar*	$2.48 \times 10^{-14} T_e^{0.33} \exp(-12.78/T_e)$	[1]
3	e + Ar → e + Ar$^+$	$2.34 \times 10^{-14} T_e^{0.59} \exp(-17.44/T_e)$	[1]
4	e + Ar* → e + Ar$^+$	$2.05 \times 10^{-13} \exp(-4.95/T_e)$	[28]
5	e + Ar* → e + Ar	2.0×10^{-13}	[28]
6	Ar* + Ar* → Ar + Ar$^+$ + e	6.2×10^{-16}	[28]

Moreover, the influence of the sheath stochastic heating [1] on the plasma bulk is taken into account, as boundary condition of the axial electron energy flux at the bulk-sheath interface

$$Q_{ez} = \frac{5}{2}k_B T_e \Gamma_{ez} + S_{stoc}. \tag{26}$$

Here, Γ_{ez} is the axial electron flux at the bulk-sheath interface, the stochastic heating flux along the axial direction [see appendix] is

$$S_{stoc}(t) = -2m_e n_{es}\left(\frac{m_e}{2\pi k_B T_e}\right)^{1/2}$$
$$\times u_{es}\left(\frac{\sqrt{\pi}}{4\alpha^{3/2}} - u_{es}\frac{1}{\alpha} + u_{es}^2\frac{\sqrt{\pi}}{2\alpha^{1/2}}\right), \tag{27}$$

where $\alpha = \frac{m_e}{2k_B T_e}$, n_{es} is the electron density at the sheath boundary and u_{es} is the sheath velocity.

2.4. Ion Monte-Carlo collision module

According to the spatio-temporal resolved electric field calculated by the sheath module, the IEADs on the electrode are obtained by the ion MCC module [10, 27]. The procedures are as follows. First, the positions and velocities of ions are initialized, i.e. the ions are initially distributed at the sheath edge with a Maxwellian distribution. Then, these ions move under the electric field force

$$\frac{d\mathbf{r}}{dt} = \mathbf{v}, \tag{28}$$

$$m_i\frac{d\mathbf{v}}{dt} = q_i \mathbf{E}_{s,sheath}. \tag{29}$$

Here, $\mathbf{r}$ and $\mathbf{v}$ are the position and velocity of the ions, respectively. The electric field $\mathbf{E}_{s,sheath}$ is obtained self-consistently by solving the Poisson equation in the sheath module.

Besides, these ions collide with neutral particles, and their trajectories are updated. In this work, the elastic collision and charge exchange collision between Ar$^+$ and Ar are considered. The ion MCC module runs until all the ions reach the electrode, and then statistics starts. To ensure statistical accuracy, 500 000 ions are needed in this module.

2.5. Reactions

In this work, simulations are performed in Ar discharges, and the reactions included in the model are listed in table 1.
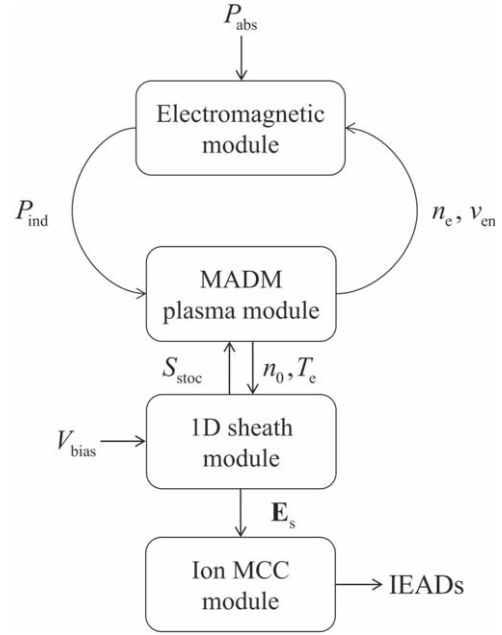
Figure 2. Flowchart of the hybrid model.

2.6. Flowchart of the hybrid model

For more clarification, the unknown parameters calculated by each module are listed in table 2.

Figure 2 shows the flowchart of the hybrid model:

(a) Based on the absorbed power P_{abs}, as well as the electron density and collision frequency from the MADM plasma module, the electromagnetic field is calculated by the electromagnetic module, and then the inductive absorbed power density P_{ind} is input into the MADM plasma module for solving the electron temperature, electron density and ion density.

(b) According to the bias voltage, as well as the radial distribution of the electron density and electron temperature at the bulk-sheath interface, the 1D sheath module is executed at each radial position. Then, the time-averaged stochastic heating flux as a function of radial position is transferred to the MADM plasma module, as boundary condition for the axial electron energy flux.

(c) These modules are coupled bi-directionally, and iteration continues until convergence is achieved.
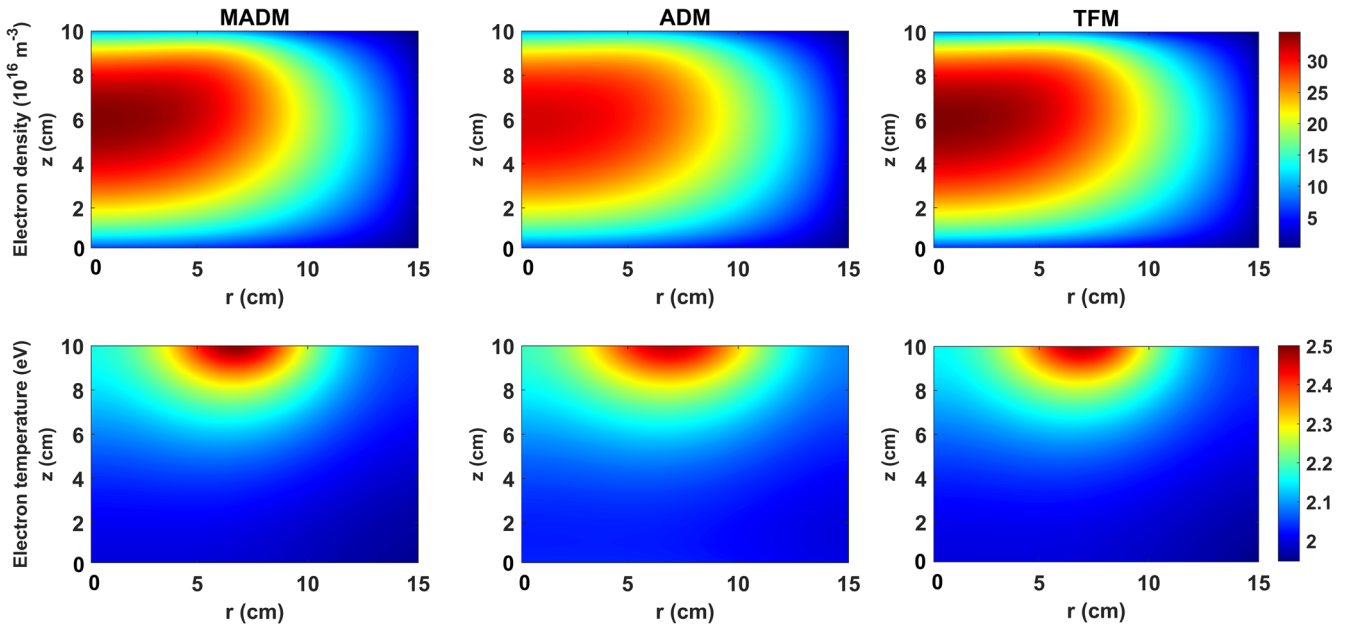
Figure 3. Two-dimensional spatial distributions of the electron density and electron temperature calculated by the three models.

Table 2. Parameters calculated by each module.

Module name	Parameter symbol	Parameter name
MADM plasma module	n_i	Ion density
	n_e	Electron density
	n_n	Neutral density
	T_e	Electron temperature
	$\mathbf{u}_i$	Ion velocity
	$\mathbf{E}_s$	Ambipolar electric field
Electromagnetic module	E_θ	Inductive electric field
	P_{ind}	Inductive deposition power density
Sheath module	$n_{e,sheath}$	Electron density in the sheath
	$n_{i,sheath}$	Ion density in the sheath
	$u_{i,sheath}$	Ion velocity in the sheath
	V	Potential in the sheath
	$\mathbf{E}_{s,sheath}$	Electric field in the sheath
	S_{stoc}	Stochastic heating flux
Ion MCC module		IEADs

(d) The spatio-temporally resolved electric field in the sheath is input into the ion MCC module, and the IEADs at different radial positions on the substrate are obtained.

3. Results and discussion

3.1. Validation of the MADM

In order to verify the accuracy and computational efficiency of the hybrid model, the results obtained by the MADM are compared with those calculated based on the TFM and ADM. The pressure is fixed at 5 Pa, the driving frequency of the coil is 13.56 MHz and the discharge power is 200 W. Since the sheath effect becomes negligible in ICP discharges without a bias source, the sheath model is not coupled with the MADM and the ADM in this subsection.

These three models run with the same initial conditions for 5000 RF cycles, and the two-dimensional spatial distributions of the electron density and electron temperature are shown in figure 3. It is clear that the electron density and electron temperature calculated by the three models have similar distributions, i.e. the electron density is the highest at the reactor center, and the maximum of the electron temperature appears below the dielectric window.

In order to detect the difference more clearly, radial distributions of the electron density and electron temperature along $z = 5$ cm calculated by the three models are plotted in figure 4. It is clear that the electron densities obtained by the MADM and TFM are almost the same, and the values are slightly higher than that calculated by the ADM, especially at the reactor center. Although the electron temperatures calculated by the three models are not the same, the discrepancy between the ADM and TFM is more apparent, indicating that the accuracy of the MADM is higher than the ADM.

The calculation time of the three different models is listed in table 3. It can be seen that the ADM and MADM could reach convergence within 10 min, because the sheath region is not simulated. However, the calculation time of the TFM is more than 5 h, which is about 45 times longer than the MADM and ADM. Indeed, the coupling between the Poisson equation and electron equations leads to strict limits on the time step, although a semi-implicit method has been applied [29]. In conclusion, by comparing with the ADM and TFM, the MADM not only guarantees the accuracy, but also shortens the calculation time.
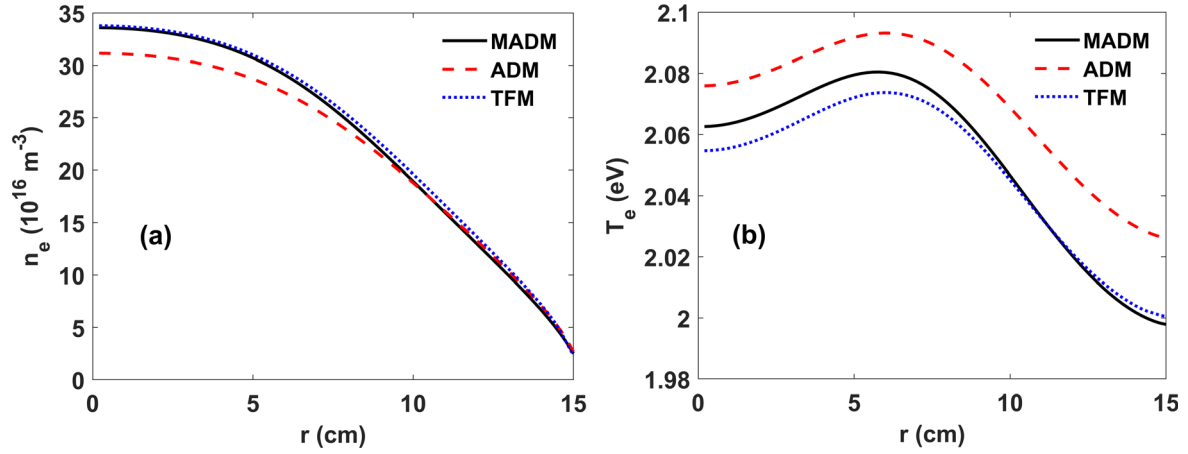
Figure 4. Radial distributions of (a) the electron density and (b) the electron temperature calculated by the three models.

Table 3. Calculation time of different models.

Models	Calculation time
ADM	6.8 min
MADM	7.0 min
TFM	5.3 h

Therefore, the hybrid model based on the MADM has been adopted to investigate the modulation of IEADs by a bias source under different discharge conditions.

3.2. Single frequency RF bias

First, a single frequency bias source is applied to the bottom electrode, and the influences of the bias voltage, bias frequency and gas pressure on the IEADs at different radial positions are investigated in ICP discharges with coil frequency of 13.56 MHz and coil power of 200 W.

Figure 5 shows the IEADs at different radial positions of the substrate for different bias voltages, i.e. 100 V, 150 V and 200 V. The bias frequency is fixed at 13.56 MHz, and the pressure is 1 Pa. Under the discharge conditions investigated, the ion energy exhibits a typical bimodal distribution. This is because on one hand, the sheath thickness is much smaller than the mean free path of ions at 1 Pa, hence ions could hardly collide with neutral species in the sheath region. On the other hand, the transit time of ions across the sheath is shorter than the RF period [15]. By increasing the bias voltage from 100 to 200 V, the energy peaks of IEADs at the same radial position move towards the higher energy, because ions could gain more energy from the higher potential drop in the sheath. Besides, the ion energy peak separation width increases with bias voltage, which is similar to that observed by experiments and simulations [15, 30].

Moreover, it is interesting to notice that the widths of the ion energy peaks at the center of the substrate ($r = 0.2$ cm) are obviously wider than that at the radial edge (i.e. $r = 14.8$ cm), indicating that the IEAD is not uniform along the
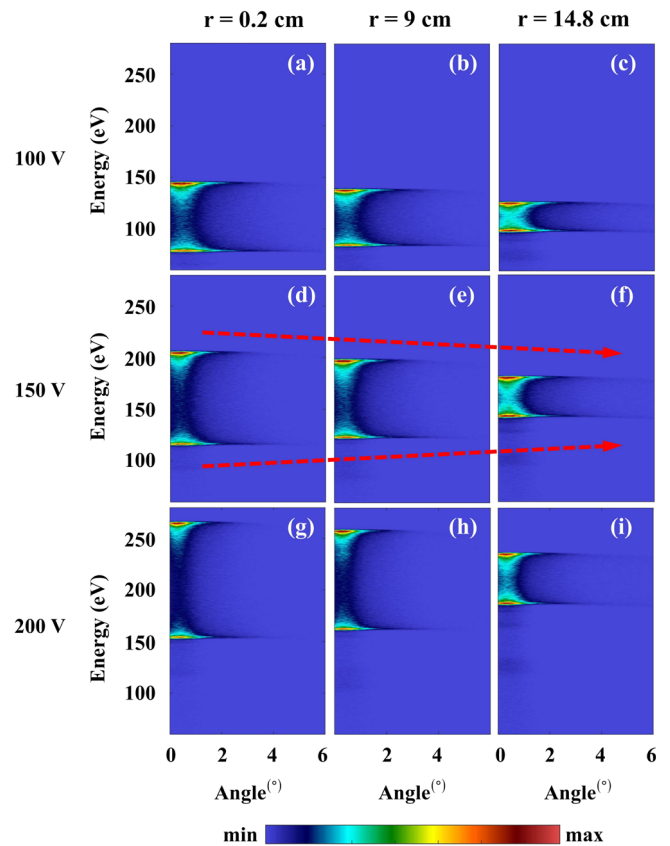

Figure 5. IEADs at different radial positions as a function of bias voltage at bias frequency of 13.56 MHz, 1 Pa.

substrate. The difference between the ion energy peak separation width can be explained by the following formula [31]

$$\Delta E = \left(\frac{8eV_{\mathrm{RF}}}{3\omega d_{\mathrm{s}}} \right) \left(\frac{2eV_{\mathrm{DC}}}{m_{\mathrm{i}}} \right)^{1/2}, \qquad (30)$$

where V_{RF} is the voltage amplitude, V_{DC} is the DC self-bias calculated by equation (24) and d_{s} is the sheath thickness. Since ΔE is inversely proportional to the sheath thickness d_{s},
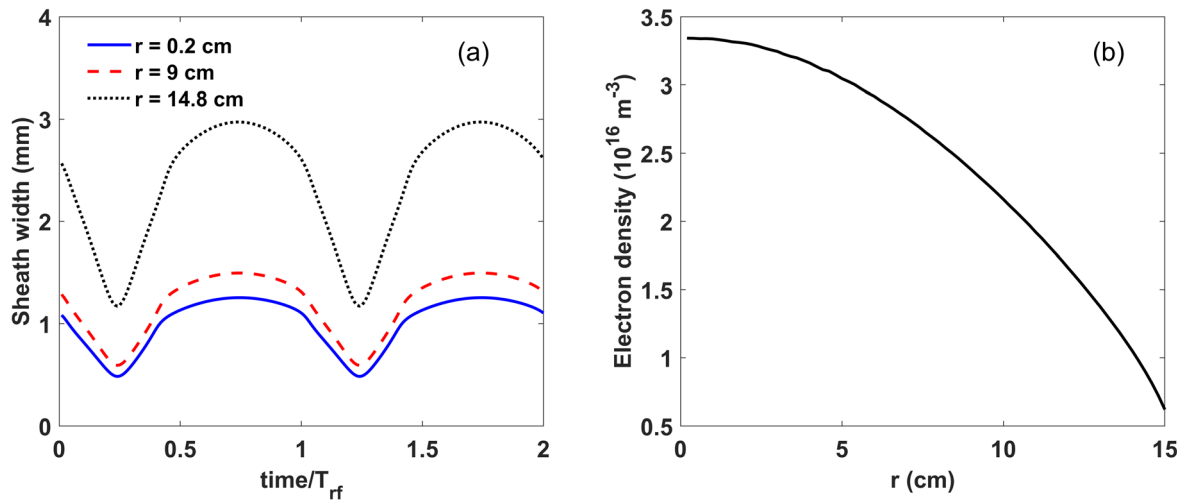
Figure 6. (a) Sheath width at different radial positions of the substrate and (b) radial distribution of the electron density at the sheath boundary, at bias frequency of 13.56 MHz, bias voltage of 100 V and 1 Pa.
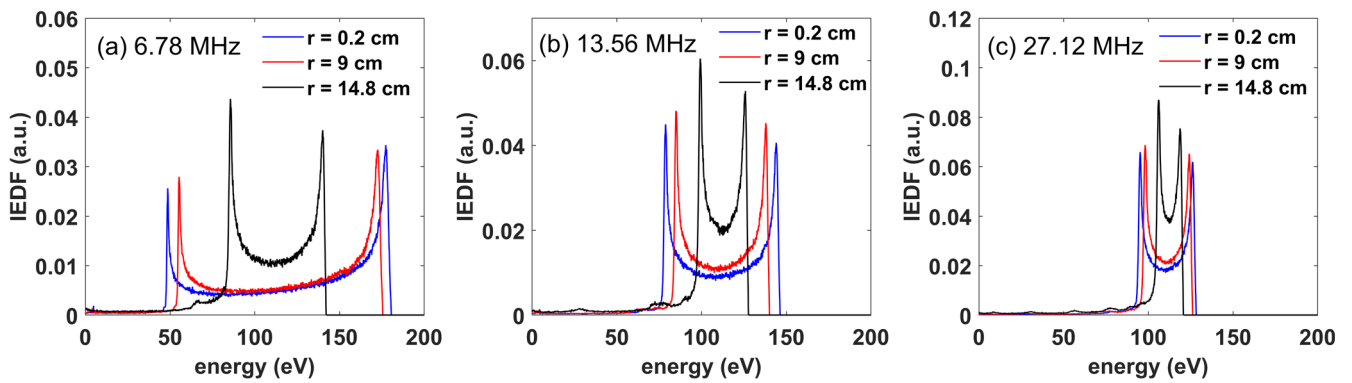

Figure 7. IEDFs at different radial positions of the substrate for different bias frequencies: (a) 6.78 MHz, (b) 13.56 MHz, and (c) 27.12 MHz, at bias voltage of 100 V and 1 Pa.

the IEAD at the radial edge becomes narrower due to the thicker sheath, as shown in figure 6(a).

Figure 6(a) shows the temporal variation of the sheath thickness at different radial positions of the substrate during one RF bias cycle, and the bias voltage is 100 V. It is clear that the sheath expands and collapses over time during one RF cycle, and the sheath at the radial edge of the substrate ($r = 14.8$ cm) is thicker than that at the radial center ($r = 0.2$ cm). This can be explained by the radial distribution of the plasma density, as shown in figure 6(b). According to the formula [1]

$$d_{\rm s} = \frac{2^{1/4}}{1.23}\left(\frac{0.82\varepsilon_0}{e}\right)^{1/2}\frac{V_{\rm DC}^{3/4}}{n_{\rm e}^{1/2}T_{\rm e}^{1/4}}, \qquad (31)$$

the averaged sheath thickness is inversely proportional to the electron density, so the sheath is thicker at the radial edge, due to the lower electron density there.

Figure 7 shows the IEDFs at different radial positions obtained at the bias frequency of 6.78 MHz, 13.56 MHz and 27.12 MHz, respectively. The bias voltage is fixed at 100 V, and the pressure is 1 Pa. It is clear that the IEDFs remain bimodal distribution and the ion energy peak separation width

at the radial center is wider than that at the radial edge for all bias frequencies investigated, due to the thinner sheath at the center, as we mentioned above. In addition, the width of the ion energy peaks decreases significantly when bias frequency increases, which is also clear from figure 8. For instance, ΔE at the radial center is 128.7 eV at 6.78 MHz, and it declines to 30.9 eV at 27.12 MHz. This is because ΔE is inversely proportional to the bias frequency (see formula (30) above). Besides, the discrepancy of ΔE at different radial positions is more obvious at lower bias frequency, indicating that the radial uniformity of IEDFs could be improved by increasing the bias frequency.

The influence of gas pressure on the IEDFs at different radial positions is presented in figure 9, at the bias frequency of 13.56 MHz and bias voltage of 100 V. When the gas pressure is 5 Pa, the IEDFs at $r = 0.2$ cm and $r = 9$ cm exhibit two obvious peaks, which is similar to that observed at 1 Pa, although there are some small low-energy peaks. This is because the ion transit times across the sheath at $r = 0.2$ cm and $r = 9$ cm are shorter than the RF period. However, at $r = 14.8$ cm, the bimodal structure of the IEDF disappears, and the IEDF is characterized by multiple low-energy peaks.
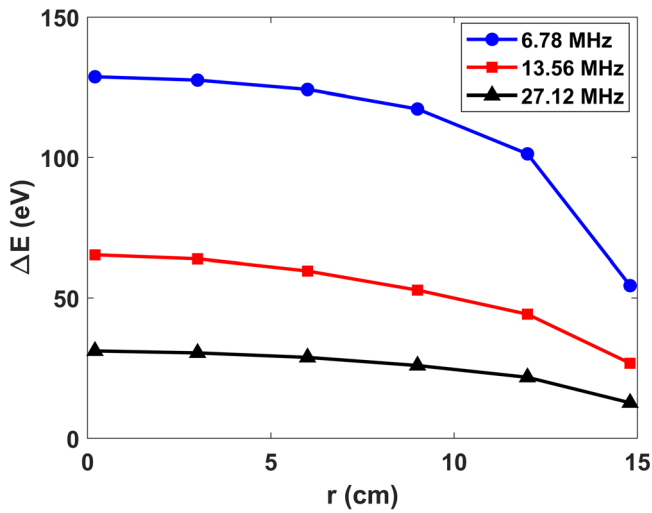
Figure 8. Evolutions of the energy peak separation width with radial position under different bias frequencies, at bias voltage of 100 V and 1 Pa.

This is because the sheath at $r = 14.8$ cm is thicker due to the lower plasma density, which results in longer time for ions to pass through the sheath. Therefore, the charge exchange collision and elastic collision between Ar^+ and Ar are sufficient, giving rise to multiple low-energy peaks in the IEDF.

When the pressure increases to 10 Pa, the IEDFs are quite different from those observed at low pressures. For instance, the IEDF at the radial center is characterized by more energy peaks instead of a bimodal distribution, and the proportion of low energy ions increases significantly. Especially at the edge of the substrate, the IEDF exhibits a multi-peak distribution and is dominated by low energy ions. This is because ions collide with neutral particles more frequently, and more neutral species become low energy ions due to the charge exchange collision. The results indicate that with the increase of gas pressure, the discrepancy of IEDFs at different radial positions becomes pronounced, which is not good for the uniformity of the etching process.

3.3. Dual frequency case

In this section, the influence of the dual frequency bias source on the IEADs is studied, at the ICP source of 13.56 MHz, 200 W, and the pressure is fixed at 1 Pa. The low frequency (LF) bias source and high frequency (HF) bias source are 13.56 MHz/100 V and 27.12 MHz/100 V, respectively, and the relative phase between them is in the range from 0 to $3\pi/2$.

Figure 10 shows the evolutions of the IEDF and IADF at the radial center with relative phase angle. It can be seen that the IEDFs in the case with dual-frequency bias source
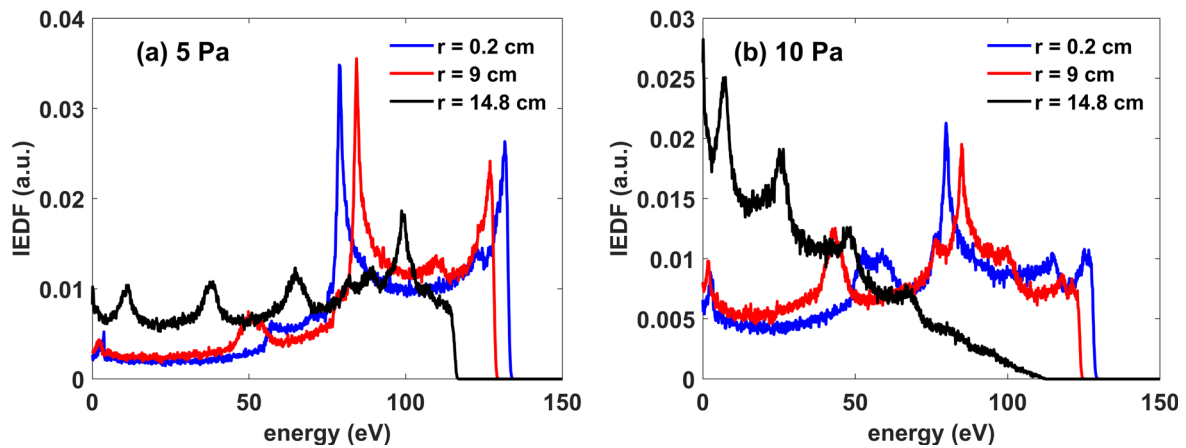

Figure 9. IEDFs at different radial positions of the substrate for different pressures: (a) 5 Pa, (b) 10 Pa, at bias frequency of 13.56 MHz and bias voltage of 100 V.
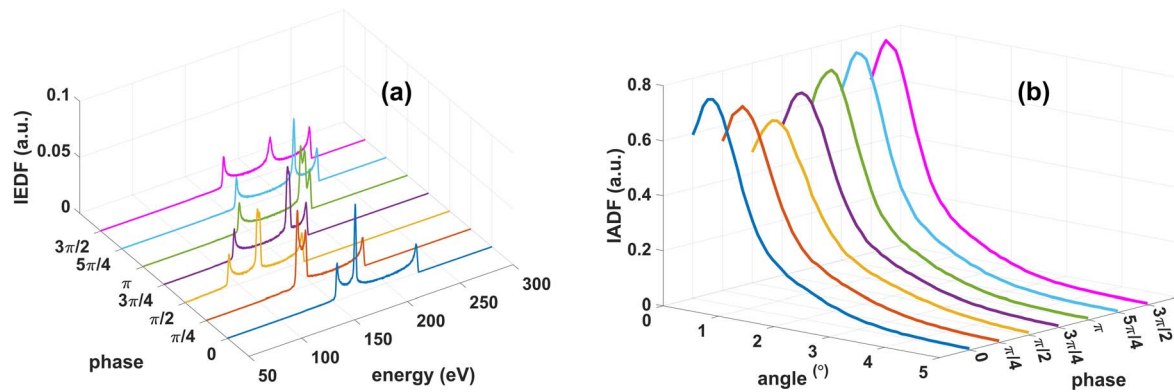

Figure 10. (a) IEDFs and (b) IADFs at the radial center for different relative phase angles.
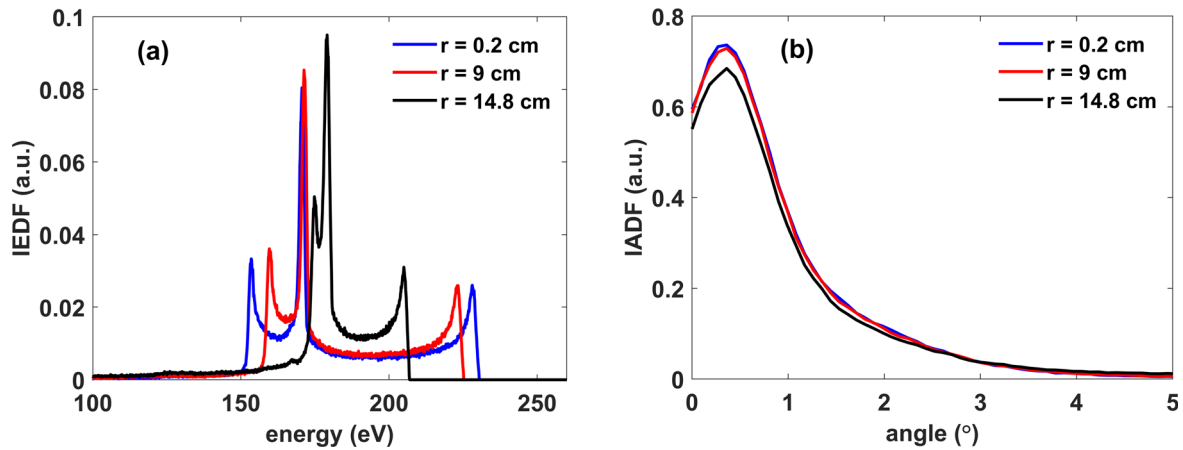
Figure 11. (a) IEDFs and (b) IADFs at different radial positions of the substrate at relative phase of 0.

are quite different from those in the single-frequency case. Indeed, when the dual frequency bias source is applied, the IEDFs have three or four energy peaks. Moreover, the modulation of the IEDF by relative phase angle is obvious. When the phase angle is 0, the IEDF exhibits three energy peaks, i.e. 153.5 eV, 170.5 eV and 228 eV, respectively, and the middle energy peak is closer to the lowest energy peak. When the relative phase increases from 0 to $\pi/2$, all the energy peaks move to the lower energy, so the average ion energy decreases. At the same time, when the phase is equal to $\pi/2$, the IEDF exhibits four energy peaks. However, as the relative phase rises further from $\pi/2$ to $5\pi/4$, all the energy peaks move to the higher energy, and the inter-mediate energy peaks are closer to the highest energy peak. Continuing to increase the phase to $3\pi/2$, the IEDF changes again to three energy peaks, and the intermediate energy peaks gradually move to the lowest energy peak. Therefore, the average ion energy first decreases and then increases as relative phase rises from 0 to $3\pi/2$, indicating that adjusting the relative phase between two bias frequencies is an effective method to modulate the IEDF. Besides, the IADF is also affected by the phase angle, i.e. the proportion of small-angle ions first decreases and then increases with relative phase.

Figures 11(a) and (b) present the IEDFs and IADFs at different radial positions of the substrate, at the relative phase of 0. When $r = 0.2$ cm, the three energy peaks appear at 154.1 eV, 171.1 eV, 227.5 eV, respectively, and the energy separation width (i.e. the width between the highest energy peak and the lowest energy peak) is the largest. At $r = 9$ cm, the middle energy peak is almost unchanged, while the lowest and highest energy peaks move close to each other, and the energy peak separation width declines to 63.7 eV. At the radial edge, i.e. $r = 14.8$ cm, the energy peak separation width is the smallest, which is similar to that observed in the single frequency bias source case. The IADFs at different radial positions exhibit similar distributions, i.e. most ions bombard the substrate at about $0.36°$ away from the vertical direction.

4. Conclusions

In this work, a modified ambipolar diffusion model is used to simulate the bulk plasma region, which could improve the computational efficiency and meanwhile ensure the accuracy. By coupling the modified ambipolar diffusion model with a 1D sheath model and an ion MCC model, the modulation of IEADs at different radial positions by bias voltage, bias frequency, gas pressure and bias voltage waveform is investigated. The results show that with the increase of bias voltage amplitude at 1 Pa, the energy peaks of the IEDF move to the higher energy, and meanwhile the width of the ion energy peaks increases. Besides, the ion energy peak separation width of the IEDF at the edge of the substrate is narrower than that at the radial center. Moreover, as the bias frequency increases, the energy peak separation width of the IEDF narrows, and the radial uniformity of the IEDF becomes better. When the gas pressure is high (such as 5 Pa and 10 Pa), the IEDF at different positions of the substrate varies greatly, which is not beneficial to the etching. In addition, when a dual-frequency bias source is applied, the IEDF changes from a bimodal structure to a multimodal structure, and the positions of energy peaks vary significantly with the relative phase between the two bias frequencies. The results obtained in this work could help to have a deep insight into the biased ICP and to optimize the etching process.

Acknowledgments

Appendix

The stochastic heating flux (equation (27)) is obtained according to the model proposed by Liebermann *et al* [1]. In

the model, the incident velocity of electrons at the sheath boundary u and the reflection velocity u_r satisfy the following relation [1]

$$u_r = -u + 2u_{es}, \qquad (A1)$$

where u_{es} is the sheath velocity.

Therefore, the power transfer is [1]

$$S_{stoc} = -2m_e \int_{u_{es}}^{\infty} u_{es}(u - u_{es})^2 f_{es}(u, t)\mathrm{d}u, \qquad (A2)$$

where m_e is the electron mass, and $f_{es}(u, t)$ is the electron velocity distribution function.

Assuming $f_{es}(u, t)$ satisfies the Maxwellian distribution, we have

$$S_{stoc} \approx -2m_e n_{es}\left(\frac{m_e}{2\pi k_B T_e}\right)^{1/2} \int_0^{\infty} u_{es}(u - u_{es})^2$$

$$\times \exp\left(-\frac{m_e u^2}{2k_B T_e}\right)\mathrm{d}u, \qquad (A3)$$

where n_{es} is the electron density at the sheath boundary, k_B is the Boltzmann constant, and T_e is the electron temperature.

Then, according to the integral formula $I(n) = \int_0^{\infty} \mathrm{e}^{-\alpha x^2}x^n \mathrm{d}x$ $(n \in \mathbb{Z}, n \geqslant 0)$, $I(0) = \frac{\sqrt{\pi}}{2\alpha^{1/2}}$, $I(1) = \frac{1}{2\alpha}$, $I(2) = \frac{\sqrt{\pi}}{4\alpha^{3/2}}$, $I(3) = \frac{1}{2\alpha^2}$, $I(4) = \frac{3\sqrt{\pi}}{8\alpha^{5/2}}$, $I(5) = \frac{1}{\alpha^3}$, we can obtain the stochastic heating flux as equation (27).

References

[1] Lieberman M A and Lichtenberg A J 2005 *Principles of Plasma Discharges and Materials Processing* (New York: Wiley) 2nd edn
[2] Lee H C 2018 *Appl. Phys. Rev.* **5** 011108
[3] Chabert P and Braithwaite N 2011 *Physics of Radio-Frequency Plasmas* (Cambridge: Cambridge University Press)
[4] Kawamura E *et al* 1999 *Plasma Sources Sci. Technol.* **8** R45
[5] Ashida S, Lee C and Lieberman M A 1995 *J. Vac. Sci. Technol.* A **13** 2498
[6] Thorsteinsson E G and Gudmundsson J T 2009 *Plasma Sources Sci. Technol.* **18** 045001
[7] Thorsteinsson E G and Gudmundsson J T 2010 *J. Phys. D: Appl. Phys.* **43** 115201
[8] Gudmundsson J T and Thorsteinsson E G 2007 *Plasma Sources Sci. Technol.* **16** 399
[9] Haidar Y *et al* 2014 *Plasma Sources Sci. Technol.* **23** 065037
[10] Wen D Q *et al* 2016 *Plasma Sources Sci. Technol.* **25** 045009
[11] Tong L *et al* 2021 *Phys. Plasmas* **28** 053512
[12] Kawamura E, Graves D B and Lieberman M A 2011 *Plasma Sources Sci. Technol.* **20** 035009
[13] Zhang Y R *et al* 2019 *J. Phys. D: Appl. Phys.* **52** 295204
[14] Kushner M J 2009 *J. Phys. D: Appl. Phys.* **42** 194013
[15] Hoekstra R J and Kushner M J 1996 *J. Appl. Phys.* **79** 2275
[16] Agarwal A and Kushner M J 2005 *J. Vac. Sci. Technol.* **23** 1440
[17] Turkoz E and Celik M 2015 *J. Comput. Phys.* **286** 87
[18] Ramamurthi B and Economou D J 2002 *J. Vac. Sci. Technol.* **20** 467
[19] Panagopoulos T *et al* 2002 *J. Appl. Phys.* **91** 2687
[20] Kropotkin A N and Voloshin D G 2020 *Phys. Plasmas* **27** 053507
[21] Bukowski J D, Graves D B and Vitello P 1996 *J. Appl. Phys.* **80** 2614
[22] Kim D and Economou D J 2003 *J. Appl. Phys.* **94** 2852
[23] Edelberg E A and Aydil E S 1999 *J. Appl. Phys.* **86** 4799
[24] Bose D, Govindan T R and Meyyappan M 2000 *J. Appl. Phys.* **87** 7176
[25] Dai Z L and Wang Y N 2002 *Phys. Rev.* **66** 026413
[26] Dai Z L and Wang Y N 2004 *Phys. Rev.* **69** 036403
[27] Nanbu K 2000 *IEEE Trans. Plasma Sci.* **28** 971
[28] Lee C and Lieberman M A 1995 *J. Vac. Sci. Technol.* **13** 368
[29] Ventzek P L *et al* 1993 *Appl. Phys. Lett.* **63** 605
[30] Gahan D, Dolinaj B and Hopkins M B 2008 *Rev. Sci. Instrum.* **79** 033502
[31] Hayden C, Gahan D and Hopkins M B 2009 *Plasma Sources Sci. Technol.* **18** 025018